

# The Critical Role of Anharmonic Lattice Dynamics for Macroscopic Properties of the Visible Light Absorbing Nitride Semiconductor CuTaN<sub>2</sub>

Franziska S. Hegner, Adi Cohen, Stefan S. Rudel, Silva M. Kronawitter, Manuel Grumet, Xiangzhou Zhu, Roman Korobko, Lothar Houben, Chang-Ming Jiang, Wolfgang Schnick, Gregor Kieslich, Omer Yaffe,\* Ian D. Sharp,\* and David A. Egger\*

Ternary nitride semiconductors are rapidly emerging as a promising class of materials for energy conversion applications, offering an appealing combination of strong light absorption in the visible range, desirable charge transport characteristics, and good chemical stability. In this work, it is shown that finite-temperature lattice dynamics in CuTaN<sub>2</sub> – a prototypical ternary nitride displaying particularly strong visible light absorption – exhibit a pronounced anharmonic character that plays an essential role in defining its macroscopic optoelectronic and thermal properties. Low-frequency vibrational modes that are Raman-inactive from symmetry considerations of the average crystal structure and unstable in harmonic phonon calculations are found to appear as intensive Raman features near room temperature. The atomic contributions to the anharmonic vibrations are characterized by combining Raman measurements with molecular dynamics and density functional theory calculations. This analysis reveals that anharmonic lattice dynamics have large ramifications on the fundamental properties of this compound, resulting in uniaxial negative thermal expansion and the opening of its bandgap to a near-optimal value for solar energy harvesting. The atomic-level understanding of anharmonic lattice dynamics, as well as the finding that they strongly influence key properties of this semiconductor at room temperature, have important implications for design of new functional materials, especially within the emerging class of ternary nitride semiconductors.

## 1. Introduction

Finite-temperature atomic motions can have a profound influence on the functional properties of energy materials, including their electronic, ionic, and thermal transport characteristics, as well as their electronic structures, phase stabilities, and defect-assisted recombination processes.<sup>[1]</sup> Thus, elucidation of atomic scale structural dynamics is of critical importance for understanding and controlling the excitations and interactions of such materials under device-relevant operational conditions. Descriptions of the lattice dynamics are normally rooted in the harmonic approximation, assuming a well-defined potential energy minimum of the crystal structure with small atomic displacements at finite temperature, which are described by a second-order Taylor expansion.<sup>[2]</sup> The resulting physical picture of non-interacting, harmonic phonons has been instrumental in rationalizing the finite-temperature behavior of classical inorganic semiconductors.<sup>[1,3]</sup> More

F. S. Hegner, M. Grumet, X. Zhu, C.-M. Jiang, I. D. Sharp, D. A. Egger  
Physics Department  
TUM School of Natural Sciences  
Technical University of Munich  
James-Franck-Straße 1, 85748 Garching, Germany  
E-mail: [sharp@wsi.tum.de](mailto:sharp@wsi.tum.de); [david.egger@tum.de](mailto:david.egger@tum.de)

F. S. Hegner, C.-M. Jiang, I. D. Sharp  
Walter Schottky Institute  
Technical University of Munich  
Am Coulombwall 4, 85748 Garching, Germany  
A. Cohen, R. Korobko, O. Yaffe  
Department of Chemical and Biological Physics  
Weizmann Institute of Science  
Rehovot 76100, Israel  
E-mail: [omer.yaffe@weizmann.ac.il](mailto:omer.yaffe@weizmann.ac.il)  
S. S. Rudel, W. Schnick  
Department of Chemistry  
Ludwig-Maximilians-Universität München  
Butenandtstr. 5-13 (D), 81377 Munich, Germany

 The ORCID identification number(s) for the author(s) of this article can be found under <https://doi.org/10.1002/aenm.202303059>

© 2024 The Authors. Advanced Energy Materials published by Wiley-VCH GmbH. This is an open access article under the terms of the [Creative Commons Attribution](https://creativecommons.org/licenses/by/4.0/) License, which permits use, distribution and reproduction in any medium, provided the original work is properly cited.

DOI: 10.1002/aenm.202303059

recent work has highlighted that atomic motions transcending the harmonic phonon picture can heavily influence the optoelectronic properties of many different classes of emerging semiconductors, including organic crystals,<sup>[4]</sup> halide perovskites<sup>[5–16]</sup> and both metal oxides<sup>[17–19]</sup> and chalcogenides.<sup>[20,21]</sup> Indeed, updated microscopic understanding is now being generated to elucidate how more complicated atomic motion – captured in the framework of anharmonic lattice dynamics – can trigger interesting consequences for key physical quantities, such as the fundamental bandgap,<sup>[5,6,12,14,15]</sup> structural phase transitions,<sup>[22–24]</sup> and nature of quasi-particle excitations.<sup>[21,25]</sup>

Ternary nitride semiconductors are fascinating materials and offer a versatile range of desirable properties for sustainable energy conversion, including solar energy harvesting, thermoelectrics, and solid-state lighting.<sup>[26–29]</sup> Compared to intensively studied metal oxide compounds, nitrides offer narrower bandgaps for efficient light absorption, along with increased covalent character that can enhance long-range charge transport. However, exploration of ternary nitrides remains in its infancy, with far fewer nitride compounds experimentally investigated than analogous oxides.<sup>[28–30]</sup> This comparatively slow pace of discovery is primarily due to challenges in synthesizing these compounds, which requires activating nitrogen. In addition, the strong N<sub>2</sub> triple bond (945 kJmol<sup>-1</sup> vs. 498 kJmol<sup>-1</sup> for O<sub>2</sub>)<sup>[26]</sup> renders many of these materials metastable. Notable examples of such metastable compounds include binary copper nitride (Cu<sub>3</sub>N)<sup>[31]</sup> and tin nitrides (Sn<sub>3</sub>N<sub>4</sub> and SnN<sub>1–δ</sub>),<sup>[32,33]</sup> and ternary tin titanium nitride (Sn<sub>1–x</sub>Ti<sub>x</sub>N<sub>4</sub>)<sup>[34]</sup> and copper tantalum or niobium nitride (CuTa<sub>2</sub>N<sub>2</sub> and CuNb<sub>2</sub>N<sub>2</sub>),<sup>[35,36]</sup> all of which offer desirable bandgaps with relevance for photovoltaic and photo(electro)catalytic energy conversion.<sup>[28,37]</sup> Despite this metastability, such compounds can exhibit extreme kinetic stabilities under operating conditions.<sup>[37]</sup> Anharmonic lattice dynamics are expected to play an important role in such nitride semiconductors and establishing an atomic-scale understanding of their underlying phase stabilities and transformations will significantly advance their technological progress.

Among the ternary nitride semiconductors reported to date, a particularly interesting compound is copper tantalum nitride, CuTa<sub>2</sub>N<sub>2</sub>, which exhibits promising properties for solar and thermoelectric energy conversion.<sup>[35,38]</sup> It is characterized by a sharp optical absorption onset at approximately 1.5 eV,<sup>[35]</sup> which is close to the optimal value for photovoltaic materials,<sup>[39]</sup> along with a remarkably large absorption coefficient (>10<sup>5</sup>–10<sup>6</sup> cm<sup>-1</sup>). CuTa<sub>2</sub>N<sub>2</sub> crystallizes in the delafossite structure, which is a layered phase that is common for many technologically relevant oxides, such as CuFeO<sub>2</sub>. Such delafossite oxides tend to possess large and anisotropic carrier effective masses, which have hin-

dered their development for solar energy harvesting.<sup>[40]</sup> In contrast, nitride delafossites are predicted to exhibit high electronic conductivities.<sup>[38]</sup> Furthermore, electronic structure calculations have revealed that the valence band (VB) comprises significant Cu *d*-orbital character, suggesting a propensity for native p-type conductivity.<sup>[37]</sup>

While this combination of optoelectronic properties suggests that CuTa<sub>2</sub>N<sub>2</sub> and related delafossite nitrides are well suited for solar energy harvesting, it has been reported to be metastable with respect to decomposition into Ta<sub>3</sub>N<sub>5</sub>, Cu, and N<sub>2</sub>. Nevertheless, it can be synthesized and possesses large cohesive energies that are comparable to oxides, making it thermally and chemically stable up to 250 °C in air, which is suitable for solar cell applications.<sup>[35]</sup> In addition, Szymanski et al. used first-principles calculations to show that the delafossite phase of CuTa<sub>2</sub>N<sub>2</sub> is unstable at low temperatures and suggested that it is dynamically stabilized at room temperature.<sup>[41]</sup> Although this is expected to have a substantial impact on the fundamental material characteristics, there are only few studies on the lattice-dynamical properties of CuTa<sub>2</sub>N<sub>2</sub> or, for that matter, the broader range of nitride semiconductors. Thus, there is a critical lack of mechanistic understanding of anharmonic vibrations and their roles in defining functional properties in these increasingly important materials.

In this work, we investigate the anharmonic lattice dynamics and their consequences for macroscopic physical properties in CuTa<sub>2</sub>N<sub>2</sub>, providing atomic-scale insight into dynamic instabilities and their roles in defining the functionality of this visible-light absorbing semiconductor. We analyze the structural fluctuations and to which degree the atomic motions deviate from the harmonic phonon picture through the combination of first-principles molecular dynamics (MD) and low-frequency Raman spectroscopy. We find particularly pronounced anharmonic dynamics involving Ta and Cu vibrations, which manifest as vibrational instabilities in low-temperature phonon dispersions and lead to intense low-frequency Raman responses at higher temperatures. At the macroscale, these anharmonic modes lead to a uniaxial negative thermal expansion (NTE) that is significantly more pronounced than in delafossite oxides. Of particular relevance to solar energy harvesting, anharmonic structural dynamics are responsible for a considerable opening of the bandgap, resulting in an absorption onset near the optimal value for photovoltaic and photoelectrochemical energy conversion. Together, these results highlight the importance of anharmonic structural dynamics in defining key properties of this emerging ternary nitride compound.

## 2. Results and Discussion

### 2.1. Synthesis and Structural Characterization

In this work, we prepared CuTa<sub>2</sub>N<sub>2</sub> by an ion-exchange reaction from NaTa<sub>2</sub>N<sub>2</sub> and CuI following a modified literature procedure (see Experimental Section).<sup>[35,42]</sup> CuTa<sub>2</sub>N<sub>2</sub> was previously described to crystallize in the high-symmetry delafossite structure (rhombohedral 3R polytype),<sup>[35,42]</sup> adopting the space group *R* $\bar{3}m$  (No. 166 in the International Tables for Crystallography).<sup>[43]</sup> Figure 1a,b show schematic representations

S. M. Kronawitter, G. Kieslich  
Chemistry Department  
TUM School of Natural Sciences  
Technical University of Munich  
Lichtenbergstraße 4, 85748 Garching, Germany  
L. Houben  
Department of Chemical Research Support  
Weizmann Institute of Science  
Rehovot 7610001, Israel

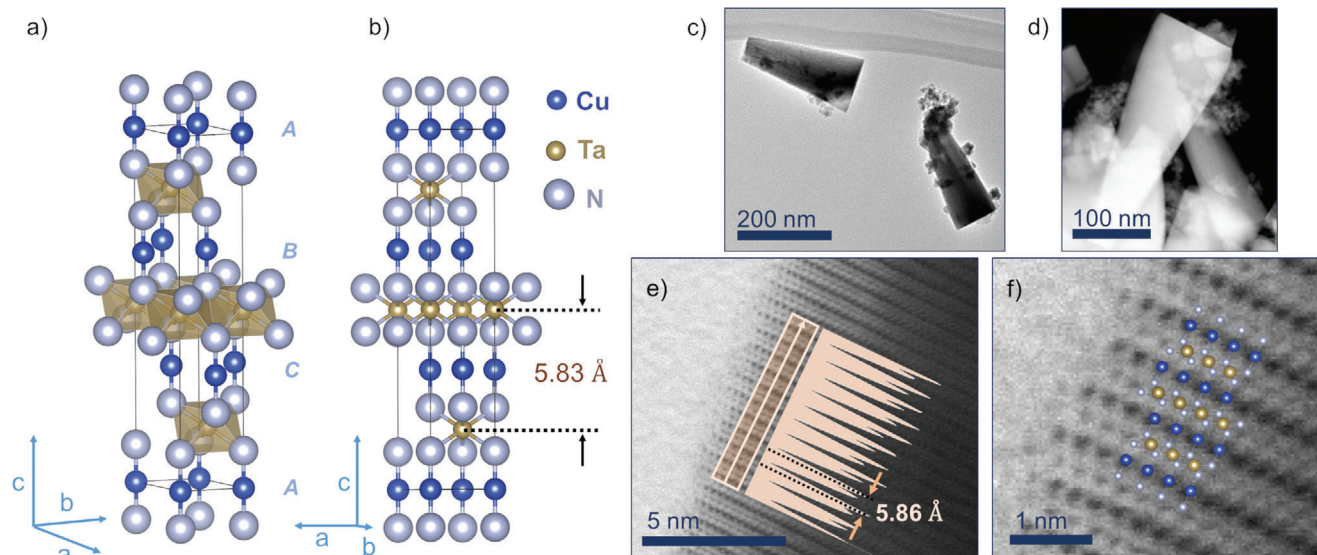


**Figure 1.** a–b) Schematic representations of the delafossite structure of  $\text{CuTa}_2\text{N}_2$  in its conventional cell representation, as optimized in density functional theory (DFT). The letters A, B, C, A in light blue indicate the stacking sequence of Cu layers. c–f) Transmission electron microscope (TEM) images of  $\text{CuTa}_2\text{N}_2$ : c) trapezoidal morphology of the  $\text{CuTa}_2\text{N}_2$  crystallites, d) scanning TEM high-angle annular dark-field (HAADF) image, e, f) high-resolution scanning TEM bright-field images from within an individual nanocrystal. Panel (e) includes the line profile generated from the image contrast and measured along the  $c$ -axis of the lattice, indicating a distance of  $5.86 \text{ \AA}$  between peaks. This value corresponds well to the DFT-calculated interplanar distance of  $5.83 \text{ \AA}$  reported in panel (b). Panel (f) includes a superimposed schematic representation of the DFT-calculated crystal structure, showing good correspondence between calculated and experimental structures.

of the delafossite  $\text{CuTa}_2\text{N}_2$  crystal structure. The atomic arrangements consist of planes of  $\text{Ta}^{5+}$  cations within edge-sharing  $\text{Ta}_6$  octahedra connected by closely-packed linear N–Cu–N bonds between  $\text{N}^{3-}$  double layers linked by monovalent  $\text{Cu}^{1+}$  ions in an ABCABC stacking sequence in the conventional unit-cell representation. Given the transition metal  $\text{Cu}^{1+} d^{10}$  and  $\text{Ta}^{5+} d^0$  orbital occupation,  $\text{CuTa}_2\text{N}_2$  exhibits semiconducting character. We can confirm the delafossite crystal structure by powder X-ray diffraction (PXRD) measurements and compare them to geometry optimizations performed with density functional theory (DFT), as well as to literature data,<sup>[35,41,42]</sup> to find small (<1%) deviations of the lattice constants (see Table S2, Supporting Information). However, as will be discussed later, a lower-symmetry structure with a very similar XRD pattern might be present at room temperature.

Transmission electron microscopy (TEM) images (Figure 1c–f) reveal that  $\text{CuTa}_2\text{N}_2$  crystallizes in a trapezoidal, cone-shaped morphology (Figure 1c,d) of 200–300 nm length and 50–100 nm diameter. The crystallites are found to be near-stoichiometric by energy dispersive X-ray (EDX) analysis within the accuracy of the method (Figure S4, Supporting Information), with very small oxygen content that likely originates from mild surface hydrolysis. In addition, we observe the presence of a secondary phase of amorphous particles (Figure 1c,d; Figure S5, Supporting Information), which are attributed to traces of the starting material and intermediate structures generated during synthesis (Table S3, Supporting Information). The interplanar distance seen in high-resolution images (Figure 1e,f) and extracted from the line profile (Figure 1e), is  $5.86 \text{ \AA}$ , which corresponds well with the calculated interlayer spacing between Cu or Ta layers of  $5.83 \text{ \AA}$  from DFT.

## 2.2. Harmonic Lattice Dynamics

Figure 2a shows the DFT-computed phonon dispersion relation and atom-resolved vibrational density of states (VDOS) of  $\text{CuTa}_2\text{N}_2$  in the delafossite phase (see Section S2, Supporting Information for further details on the harmonic modes). Despite successful experimental synthesis of this material, the presence of imaginary modes indicates that this phase is unstable at 0 K.<sup>[44]</sup> Szymanski et al. previously suggested that  $\text{CuTa}_2\text{N}_2$  is dynamically stabilized at room temperature<sup>[41]</sup> but the mechanisms of this dynamic stabilization remained unclear. Here, we begin by resolving the atomic motions underlying the instability at 0 K. Inspection of the VDOS in Figure 2a reveals that the imaginary modes, labeled here as Mode 1 and Mode 2, can be primarily attributed to Ta and Cu vibrations. Visualization of the corresponding mode eigenvectors shows an “up-down” (along  $c$ -axis) motion of Ta atoms (Mode 1, see Figure 2b) and a “sideways” (along  $ab$ -plane) motion of Cu atoms (Mode 2, see Figure 2c). We note that, while we describe the atomic motions at the  $L$ -point here, the imaginary modes in other regions of the Brillouin zone consist of similar Ta and Cu motions or a superposition thereof (see Figure S8, Supporting Information).

To investigate the consequences and implications of these instabilities, we next compute the potential energy changes associated with the atomic motions underlying these two imaginary modes. Figure 2b,c show that displacements along both Mode 1 and Mode 2 lead to anharmonic double-well potentials, which are typical for dynamic instabilities. These double-wells indicate that motion along either Mode 1 or Mode 2 will stabilize the structure. The potential-well depth is much deeper (by a factor of  $\approx 50$ ) for Mode 1, which suggests that the corresponding Ta up-down

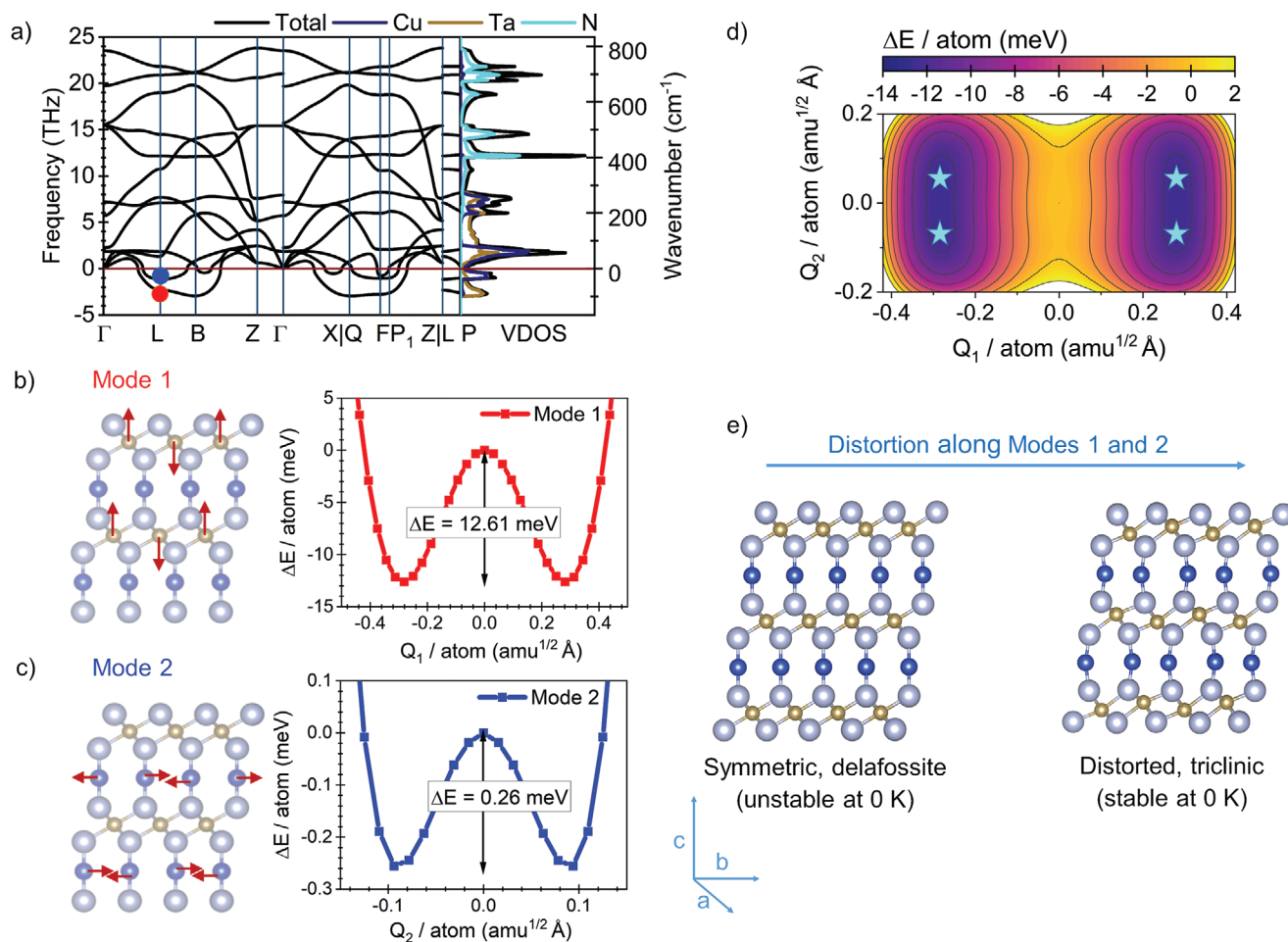


**Figure 2.** a) DFT-calculated phonon dispersion relations and atom-resolved vibrational density of states (VDOS) of  $\text{CuTaN}_2$ . We obtain two imaginary modes, Mode 1 (red) and Mode 2 (blue), which are depicted as negative frequency modes. b,c) Illustrations of the atomic motions along b) Mode 1 and c) Mode 2, together with the corresponding 1D energy profiles of these modes. The latter were obtained by displacing atoms along their mode eigenvectors at the  $L$ -point of the Brillouin zone. d) 2D map showing the energy changes associated with exciting both imaginary modes of the static delafossite structure, with stars indicating the energetic minima. e) Schematic representation of the DFT-optimized symmetric and distorted structures. (Color code: Cu: blue; Ta: gold; N: grey).

motion will be dominant in stabilizing the structure. Similarly, the Ta displacement, at which the minimum energy occurs, is much larger ( $\approx 0.3 \text{ amu}^{1/2} \text{ \AA}$ ) than the Cu displacement ( $\approx 0.1 \text{ amu}^{1/2} \text{ \AA}$ ). Such double-well characteristics were previously found in other important material classes such as halide perovskites<sup>[45–47]</sup> and lead chalcogenides,<sup>[48,49]</sup> where they significantly impact the bandgap,<sup>[14,15,45,50]</sup> ferroelectricity,<sup>[46]</sup> and electronic<sup>[9,16]</sup> and thermal<sup>[49,51]</sup> conductivities. However, to the best of our knowledge, such a potential energy landscape and its link to functional material properties has not yet been reported for ternary nitride semiconductors.

These results further confirm that the high-symmetry, rhombohedral  $R\bar{3}m$  phase of  $\text{CuTaN}_2$  is not a minimum in the potential energy surface at 0 K.<sup>[52]</sup> To obtain the ground-state structure of  $\text{CuTaN}_2$ , we construct a 2D-map of the potential energy surface associated with excitation of vibrational Modes 1 and 2, starting from the ideal, symmetric delafossite structure, as shown in Figure 2d. We find that Ta up-down and less-pronounced Cu sideways motions lead to a stabilization by triclinic distortions of

$\text{CuTaN}_2$ . We reoptimized this structure to find the global minimum of the potential energy surface at 0 K, which is henceforth referred to as distorted structure (Figure 2e). The properties of the triclinic, distorted structure are provided in Table S5 (Supporting Information). The imaginary phonons disappear for this distorted structure (Figure S10, Supporting Information), confirming that it represents the true energetic minimum and is stable at 0 K.

### 2.3. Anharmonic Lattice Dynamics at Room Temperature

The above-described indicators for the presence of anharmonic lattice dynamics in  $\text{CuTaN}_2$  motivate an investigation of vibrational anharmonicities in this material at ambient conditions. Indeed, comparing the room-temperature Raman spectrum to results from lattice dynamics calculations based on DFT (see Figure 3a, top panel) immediately reveals that the vibrational properties at ambient conditions cannot be described within the

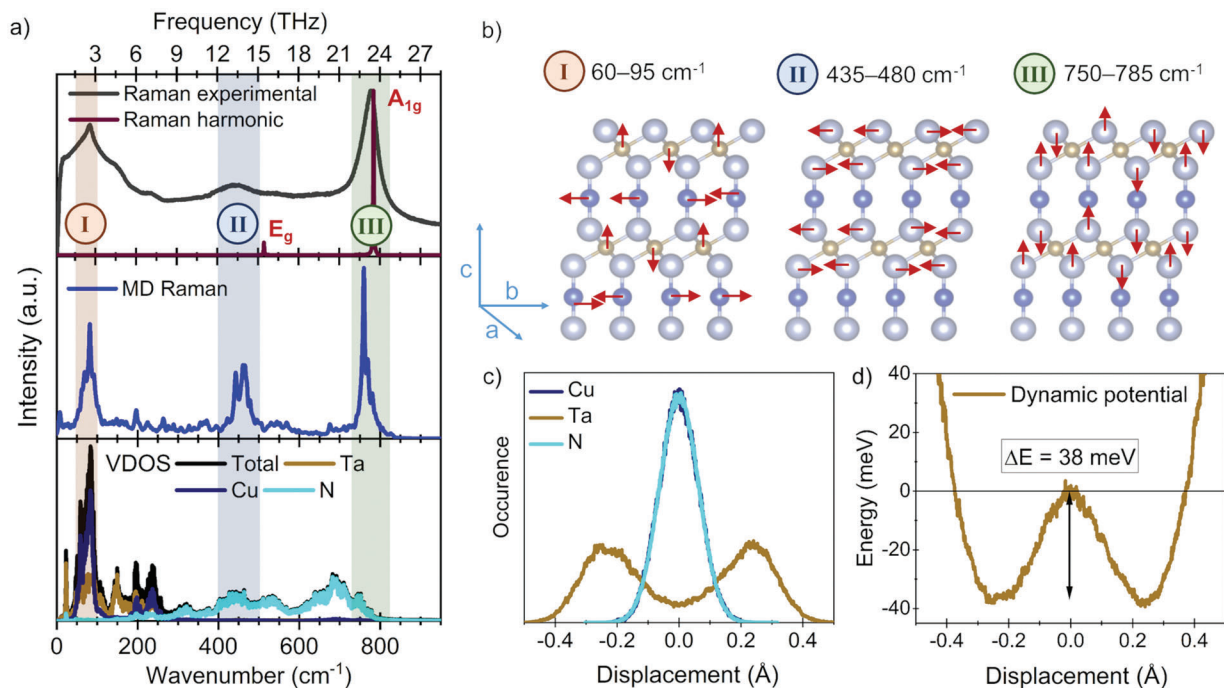


**Figure 3.** a) Comparison of experimental and computational vibrational spectra of  $\text{CuTaN}_2$ . Top: Raman spectrum measured at room temperature (grey) with the DFT-computed Raman intensities obtained from the harmonic modes at 0 K (shown in red). Middle: Raman intensities obtained from MD-Raman at 300 K. Bottom: Atom-resolved VDOS calculated from MD at 300 K. Three frequency intervals I, II, and III are indicated by shaded regions corresponding to b) illustrations of the atomic motions appearing in each frequency interval. (Color code: Cu: blue; Ta: gold; N: grey) c) Histogram of atomic displacements referenced to the equilibrium structure along the  $c$ -axis during the MD trajectory at 300 K. d) Dynamic potential energy well corresponding to Ta displacements along  $c$  obtained in MD calculations at 300 K.

harmonic approximation. Specifically, from factor group analysis one would expect two Raman active modes, the  $E_g$  and the  $A_{1g}$  mode. These modes correspond to symmetric stretches of the Ta–N bonds of the  $\text{TaN}_6$  octahedra and the symmetric stretch of the Cu–N bonds of the linear  $\text{CuN}_2$  units, respectively (Figure S6, Supporting Information). The results from harmonic lattice dynamics calculations indeed confirm this expectation. However, while these modes appear in the experimental Raman spectrum near  $450\text{ cm}^{-1}$  ( $E_g$ , labeled as Region II) and  $780\text{ cm}^{-1}$  ( $A_{1g}$ , labeled as Region III), they cannot be described by Lorentzian line-shapes. This stands in contrast to expectations for harmonic, first-order Raman-active vibrations. Furthermore, the measured Raman spectrum exhibits pronounced scattering intensity at low frequencies ( $60\text{--}95\text{ cm}^{-1}$ , labeled as Region I in Figure 3a), which is not predicted by the harmonic model. Together with similar results from infrared (IR) absorption measurements (Figure S9, Supporting Information), these findings conclusively reveal that anharmonic lattice dynamics are active in  $\text{CuTaN}_2$  at room temperature.

To investigate the anharmonic atomic motions theoretically, we now turn to DFT-based MD. In contrast to harmonic phonon procedures, this method fully captures anharmonicity in the semiclassical treatment of the atoms. In particular, we employ an “MD-Raman” approach where the Raman spectrum is obtained from correlation-function analysis of the polarizability timeseries from the MD trajectory<sup>[53]</sup> (see Computational Methods). The anharmonic Raman spectrum at 300 K (see Figure 3a, middle panel) corresponds well with the experimental one and can

also be grouped into three main regions. Applying a “frequency-filter” (see Computational Methods) to depict the atomic motions associated with these regions, we find that Region II involves sideways and Region III up-down motions of N (see Figure 3b). This is in line with expectations borne from our harmonic calculations for the appearance of  $E_g$  and  $A_{1g}$  modes described above, as well as with the finding that the atom-resolved VDOS shows contributions only from N at frequencies  $>300\text{ cm}^{-1}$  (see Figure 3a, bottom panel). Remarkably, the low-frequency Region I features atomic motions akin to the lattice instabilities that appeared as imaginary modes in the harmonic phonon dispersion (*cf.* Figure 2b,c). Specifically, it is found to contain up-down motions of Ta, as well as sideways motions of Cu, which coincides with the motions along Mode 1 and Mode 2 eigenvectors that were discussed above (*cf.* Figure 2b,c). We also computed the harmonic, first-order Raman spectrum of the distorted  $\text{CuTaN}_2$  phase (Figure S11, Supporting Information), and found that these low-frequency vibrations are present there. However, their intensity is extremely small and, thus, cannot fully explain the pronounced Raman features seen in the experimental and MD-Raman data (*cf.* Figure 3a). This suggests a large degree of anharmonicity involving phonon–phonon coupling, i.e., coupling between the low-frequency Ta and Cu vibrations (as seen in Region I in Figure 3b).

The structural dynamics at 300 K can further be analyzed by plotting the statistical distributions of the finite-temperature atomic displacements away from the static, high-symmetry

structure of CuTa<sub>2</sub>N<sub>2</sub> (see Figure 3c; and Figure S14, Supporting Information). We find a non-Gaussian distribution of Ta atoms along the *c*-axis direction, with preferred atomic positions far away ( $\approx 0.26$  Å) from the high-symmetry locations, which are rarely visited dynamically. This is in sharp contrast to all Cu and N motions, as well as the Ta motions along *a* and *b*, which appear as Gaussian distributions around their high-symmetry position as expected for harmonic motions (Figure S14, Supporting Information). The energetics involved in the Ta motions along the *c*-direction were extracted by a Boltzmann-inversion technique<sup>[54]</sup> (see Figure 3d and Computational Methods for details). The procedure provides an effective potential well for the displacements that we denote as a “dynamic potential”, in contrast to the quasi-static, frozen-phonon energetics discussed above (*cf.* Figure 2). Indeed, the shape of the dynamic potential resembles the static potential well of Mode 1 (*cf.* Figure 2b) but is significantly deeper ( $\approx 38$  meV vs.  $\approx 13$  meV). Again, this suggests that anharmonic effects play a significant role and that the well depth is increased via coupling between Ta and Cu vibrations, which was also seen in the analysis of the low-frequency feature. The appearance of such double-well potentials arising with the disordered atomic motions in the lattice has previously been found to explain low-frequency features in the Raman spectrum and VDOS of different materials.<sup>[55]</sup>

The well depth of 38 meV corresponds to a thermal energy of temperature 441 K, which suggests that at 300 K Ta atoms mostly occupy either side of the double-well. This can be confirmed by inspecting the motion of individual Ta atoms in the MD (Figure S15, Supporting Information), which are found to oscillate around either  $-0.26$  Å or  $+0.26$  Å (along the *c*-direction), showing jumps to the other side of the well only occasionally. Hence, at 300 K, 50% of the Ta atoms are displaced toward negative *c* and 50% toward positive *c*, which is confirmed by the average structure extracted from MD (Figure S15, Supporting Information). One may expect to observe such a distorted structure that is similar to the MD-averaged one in PXRD, where we had found the symmetric delafossite structure. However, the theoretical XRD patterns (see Figure S12, Supporting Information) of the distorted and symmetric CuTa<sub>2</sub>N<sub>2</sub> phase show only small differences, which we cannot resolve experimentally due to the small crystallite size of powdered CuTa<sub>2</sub>N<sub>2</sub>. These findings suggest that the structure is *not* dynamically stabilized at 300 K.

We further investigated whether the bimodal Ta-distributions observed at 300 K persist at higher temperatures and performed additional MD runs at 520 K (see Section S4B, Supporting Information). We found that the distributions of Ta atoms along the *c*-direction flatten and the dynamic potential-well depth decreases with increasing temperature (Figure S16, Supporting Information). At 520 K, the Ta atoms have a higher thermal energy ( $k_B T \approx 45$  meV) available, while the well depth is reduced to 24 meV, which therefore becomes easily surmountable. In line with this, the Ta atoms were found to reside in both sides of the potential well with an almost equal likelihood, i.e., they frequently jump between positive and negative *c*-displacements (Figure S17, Supporting Information). At this temperature, the structure is truly dynamically stabilized.

## 2.4. Consequences of Anharmonic Lattice Dynamics for Macroscopic Properties

The consequences of anharmonic lattice dynamics in CuTa<sub>2</sub>N<sub>2</sub> are first investigated by variable temperature PXRD (see Figure 4a), from which the temperature-dependent lattice parameters and volumes shown in Figure 4b are extracted (see Section S1C, Supporting Information for details). We first note that the PXRD patterns at different temperatures do not change significantly. As mentioned above, the expected symmetry reduction is not directly resolved in PXRD (see Section S3D, Supporting Information for a detailed discussion). Importantly, the data reveal uniaxial negative thermal expansion (NTE) behavior along the *c*-axis, perpendicular to the nitrogen double-layers, and positive thermal expansion along the *a*- and *b*-axes, parallel to the nitrogen double-layers. The corresponding linear thermal expansion coefficients, given by  $\alpha_i = \frac{1}{l_i} \frac{\partial l_i}{\partial T}$  (with  $l_i$  being the considered lattice parameter), are  $\alpha_{a,b} = 8.42 (\pm 0.07)$  MK<sup>-1</sup> and  $\alpha_c = -2.39 (\pm 0.57)$  MK<sup>-1</sup>; the overall volume thermal expansion is positive with  $\alpha_v = 14.76 (\pm 0.87)$  MK<sup>-1</sup>.

Further insight regarding the connection between uniaxial NTE and vibrational anharmonicities in CuTa<sub>2</sub>N<sub>2</sub> is obtained by placing our findings into the context of previous work on oxide delafossites. In particular, oxides such as CuLaO<sub>2</sub> and CuScO<sub>2</sub> were previously found to exhibit similar NTE behavior,<sup>[56]</sup> though the effect in these oxides is smaller by a factor of  $\approx 2$  than the NTE for CuTa<sub>2</sub>N<sub>2</sub>. A shrinking of the O–Cu–O linkage due to the transverse motion of Cu has been discussed as a cause of this phenomenon. Our lattice-dynamics and MD calculations suggest an analogous explanation for CuTa<sub>2</sub>N<sub>2</sub> that follows the so-called tension effect (see Figure 4c).<sup>[57]</sup> That is, the temperature-activated transverse motions of Cu atoms, described above as Mode 2 (*cf.* Figure 2), were found to appear at low frequencies and to involve small energy barriers. With these Cu motions appearing along the *b* (= *a*) direction, the N–Cu–N distance must shrink if the Cu–N bond lengths are kept constant. Due to the strength of this chemical bond, the system tends to maintain the Cu–N bond lengths, as any change in these bond distances would raise the total energy significantly. Furthermore, the large-amplitude, up-down Ta motions involved in Mode 1 (*cf.* Figures 2 and 3) that are concurrent with the Cu sideways motions allow the structure to be flexible enough so that the N atoms instantaneously adapt to maintain the Cu–N distance. Overall, these collective atomic motions on average reduce the interlayer spacing and the crystal contracts along the *c*-direction. Here, the main contribution comes from the transverse acoustic modes (Modes 1 and 2), which typically provide the primary mechanism for structural NTE.<sup>[57]</sup> Therefore, the uniaxial NTE in CuTa<sub>2</sub>N<sub>2</sub> is a macroscopic manifestation of the specific atomic motions involved in the anharmonic lattice dynamics in this material. At first glance, it may be surprising that the magnitude of the NTE in CuTa<sub>2</sub>N<sub>2</sub> is much larger than for oxide delafossites, given that the more covalent Cu–N bonds would yield a less flexible network, which was shown to reduce the NTE effect.<sup>[58]</sup> However, the strength of the Cu–N bond, whose length needs to be preserved as much as possible during the Cu sideways motions, leads to an increase in the tension effect.

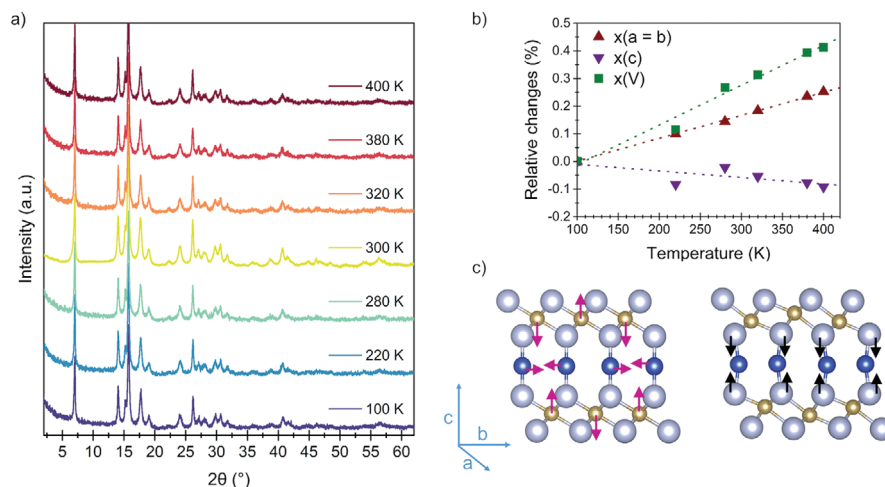


**Figure 4.** a) Temperature-dependent PXRD patterns of CuTaN<sub>2</sub> measured at ambient pressure. b) Relative changes of lattice parameters  $a$  ( $=b$ ) and  $c$ , as well as volume,  $V$ , as a function of temperature, referenced to the unit cell parameters measured at 100 K. c) Schematic illustration of the tension effect that leads to negative thermal expansion (NTE): Cu atoms move sideways (along  $a/b$ ) while Ta atoms move up and down (along  $c$ , pink arrows on the left). This leads to a structural distortion (depicted on the right), where N atoms approach each other (black arrows), keeping the Cu–N bond length constant and, thus, shrinking the  $c$ -axis. (Color code: Cu: blue; Ta: gold; N: grey).

In view of the profound consequences of thermal atomic motions and vibrational anharmonicities on fundamental structural properties of CuTaN<sub>2</sub>, we also assess their impact on its optoelectronic characteristics. First, we determine the optical absorption characteristics and bandgap of CuTaN<sub>2</sub> via diffuse reflectance (Figure 5a). We find an indirect bandgap of  $1.37 \pm 0.02$  eV and a direct bandgap of  $1.41 \pm 0.02$  eV (Figure 5b), in agreement with literature<sup>[35]</sup> and highlighting the suitability of CuTaN<sub>2</sub> for harvesting solar energy. Theoretical calculations performed for the symmetric delafossite structure, employing the HSE hybrid exchange–correlation functional<sup>[59,60]</sup> and accounting for spin–orbit coupling (SOC), yield relatively similar values: i.e., an indirect bandgap of 1.37 eV and a direct gap of 1.68 eV at the  $L$  point (see Supporting Information for further details). As we will now show, this level of agreement between experiment and theory is merely fortuitous.

We next investigate the impact of the anharmonic lattice dynamics on the bandgap. Figure 5c compares the average bandgap of CuTaN<sub>2</sub> computed along the MD trajectory to the one of the high-symmetry ( $R\bar{3}m$ ) structure calculated at 0 K using DFT. A relatively large opening of the bandgap by +0.4 eV is found in the MD calculations. In particular, the MD-averaged gap is found to be 0.82 eV while the static gap amounts to only 0.44 eV (both calculated at the PBE-DFT level without considering SOC). These results provide a strong indication that dynamic atomic effects play a crucial role in defining the bandgap of this material.

To better assess the role of anharmonic lattice dynamics on the electronic structure, we next chose a representative sample of structures with bandgaps close to the average one – calculated with the PBE functional – in order to perform more accurate but also computationally more demanding hybrid-functional DFT calculations. Here, we assume that the bandgaps evaluated with the two levels of computational methods correlate linearly.<sup>[61]</sup> Using these structures, we recomputed the bandgaps with an HSE+SOC approach and obtained a value of  $\approx 1.7$  eV for the fun-

damental gap at room temperature. This value is slightly higher than the experimentally determined onset of optical absorption (from our measurements and literature data)<sup>[35]</sup> for CuTaN<sub>2</sub>. This is expected given that we compute the fundamental gap without considering possible excitonic effects, and HSE gap can show deviations to experimental ones. Furthermore, we applied a frequency-filter to the MD trajectory in order to compute bandgaps with the PBE functional for only the low-frequency vibrations ( $<100$  cm<sup>-1</sup>) that we identified as the most dominant ones in the anharmonic mechanism, omitting all higher-frequency components in the MD. Interestingly, this procedure yields a virtually identical average bandgap to the one computed using the full MD. Conversely, when these low-frequency vibrations are omitted, and we filter the MD data to consider only atomic motions appearing at frequencies  $>100$  cm<sup>-1</sup>, the bandgap opening is significantly reduced, by 0.2 eV. Therefore, the above-described anharmonic fluctuations away from the symmetric crystal structure lead to profound changes in the electronic structure of CuTaN<sub>2</sub>, as quantified here by the bandgap.

Comparing the MD-averaged bandgap to the one of the low-symmetry, distorted structure, which we described above (see Figure 2e), the bandgap is calculated to be 1.15 eV with PBE and 2.25 with HSE, respectively (see Table S6, Supporting Information), i.e., a few hundred meVs larger than the average MD gap. The fact that the fully distorted, static structure shows an even larger bandgap opening compared to the MD-averaged one again confirms the critical role of the atomic motions away from their lowest-energy configurations for defining the bandgap.

Figure 5d compares the electronic density of states (DOS) for the static high-symmetry and distorted structures, revealing substantial differences between the two. A detailed assessment of the electronic structure is given in the Supporting Information (Figures S17 and S18, Supporting Information). The valence band is mainly composed of Cu–N antibonding orbitals, which likely renders CuTaN<sub>2</sub> tolerant to defects, an important attribute for potential technological applications.<sup>[62]</sup> The triclinic

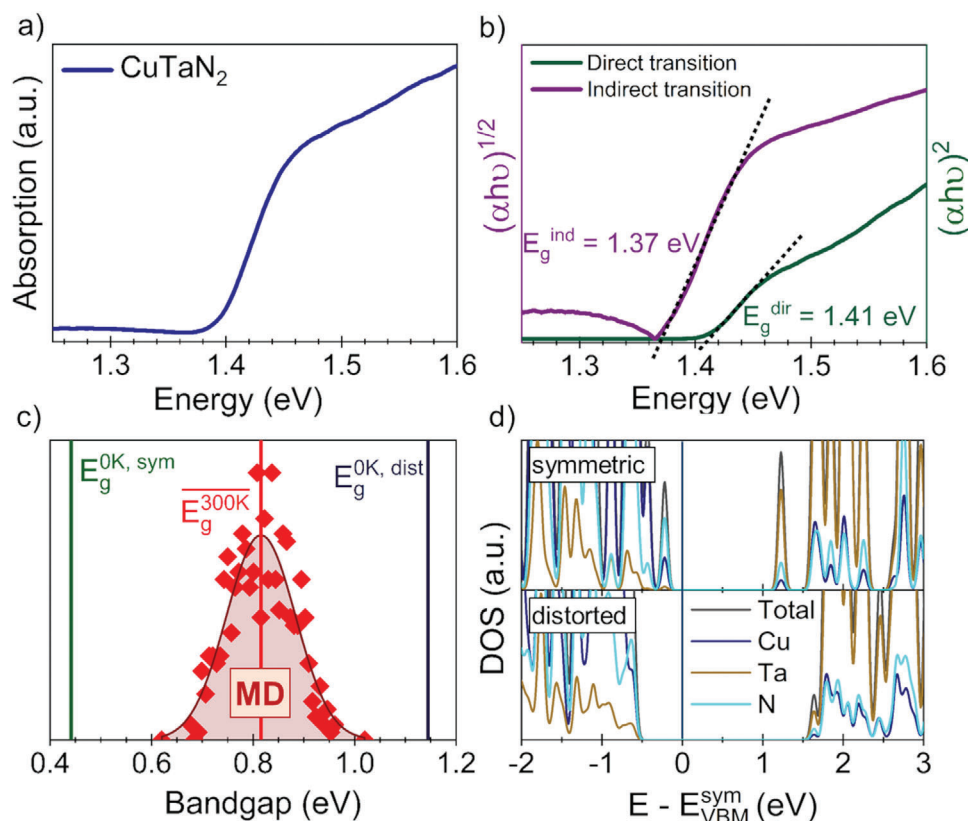


**Figure 5.** a) UV-vis absorption spectrum and b) corresponding Tauc fits. c) Bandgap distribution of CuTa<sub>2</sub>N<sub>2</sub> at 300 K (red) obtained from 600 snapshots along the MD trajectory, including a Gaussian fit as a guide to the eye. The PBE bandgaps of the static symmetric and distorted structures at 0 K are shown by green and dark blue vertical lines, respectively. d) Densities of states (DOSs) of the symmetric (top) and distorted (bottom) structures, computed with HSE. The energy eigenvalues were referenced to the N 2s level and aligned to the valence band maximum (VBM) of the symmetric structure ( $E_{VBM}^{sym}$ ).

distortion of the structure lowers the valence band maximum, which we ascribe mainly to sideways motion of Cu reducing the orbital overlap and Cu–N antibonding character. The Ta up-down motion, on the other hand, is likely responsible for the significant increase of the conduction band minimum, which mainly comprises Ta *d*-states. Since we have shown that these distortions are directly connected to the anharmonic lattice dynamics occurring at 300 K, it is possible to conclude that they are responsible for the bandgap opening in CuTa<sub>2</sub>N<sub>2</sub>. We note that these dynamic changes in orbital overlaps not only impact the bandgap of the material as shown here but are likely to also modulate other key properties, such as carrier transport, as suggested by the enhanced energetic bandwidth in the distorted structure. Altogether, this demonstrates that the anharmonic lattice dynamics play a profound role in defining some of the most important optoelectronic properties of CuTa<sub>2</sub>N<sub>2</sub> for solar energy harvesting, including both optical absorption and transport characteristics.

### 3. Conclusion

In summary, we investigated the finite-temperature lattice dynamics in the metastable ternary nitride semiconductor CuTa<sub>2</sub>N<sub>2</sub>. This material is known for strong light absorption in the visible range, which is an essential property for solar energy applications. At the same time, it was previously suggested that it ex-

hibits anharmonic lattice dynamics and dynamic stabilization at higher temperatures. Here, we characterize the precise atomic contributions to the anharmonic lattice dynamics and show how they are involved in intensive Raman signals at low frequency, which are forbidden by the symmetry of the average crystal structure. The combination of Raman spectroscopy and MD, as well as DFT, allowed for rationalization of the important consequences of anharmonicity in CuTa<sub>2</sub>N<sub>2</sub>, including its negative thermal expansion and a comparatively large increase of the fundamental bandgap to a near-ideal value for solar energy harvesting. Therefore, our work demonstrates that vibrational anharmonicity is a microscopic effect which impacts macroscopic observables that are essential for the functionality of these materials. The characterization of the anharmonic lattice dynamics and their consequences for CuTa<sub>2</sub>N<sub>2</sub> have important implications for guiding future material synthesis toward new functionalities, such as solar light harvesting, within the important class of emerging ternary nitride semiconductors.

### 4. Experimental Section

**Synthesis:** CuTa<sub>2</sub>N<sub>2</sub> was obtained via an ion exchange reaction of the layered precursor NaTa<sub>2</sub>N<sub>2</sub> with CuI:



as previously described.<sup>[35,42]</sup> Pure CuI, however, melts above the proposed metathesis temperature of 400 °C. To decrease its melting point below the synthesis temperature and, thus, to achieve better diffusion, CuI was mixed with NaI. The 70% CuI / 30% NaI mixture melts at  $\approx 385$  °C and remains molten during the reaction until a concentration of NaI >40% is reached. A phase-diagram of CuI/NaI is presented in the Supporting Information (Figure S1, Supporting Information). NaTa<sub>3</sub>N<sub>5</sub> was prepared by heating Ta<sub>3</sub>N<sub>5</sub> and metallic Na placed in a copper boat with increasing temperature from 350 to 500 °C in an NH<sub>3</sub> stream. Using a copper boat inside a fused silica tube that was lined with a copper tube within the heated area proved crucial to obtain high purity CuTa<sub>3</sub>N<sub>5</sub>. When using fused silica or alumina, oxide impurities such as Na<sub>3</sub>TaO<sub>4</sub> or NaTaO<sub>3</sub> occurred because the boat and the fused silica tube were attacked during the reaction. Ta<sub>3</sub>N<sub>5</sub> was prepared by ammonolysis of TaCl<sub>5</sub> to avoid oxidic impurities from incomplete nitridation of the alternative starting material Ta<sub>2</sub>O<sub>5</sub>. A complete description of the synthesis of the precursors and intermediates, including quantities and chemical specification is given in the Supporting Information. All reactions were carried out under exclusion of air and moisture to avoid surface hydrolysis or surface oxidation. It is noted that the deposition of CuTa<sub>3</sub>N<sub>5</sub> by reactive co-sputtering has also been attempted over a broad range of conditions, similar to those that enable formation of binary Ta<sub>2</sub>N<sub>3</sub><sup>[63]</sup> and Ta<sub>3</sub>N<sub>5</sub>.<sup>[64]</sup> However, those attempts were not successful and instead yielded mixed phase films comprising Ta<sub>3</sub>N<sub>5</sub> and metallic Cu, consistent with the known metastability of CuTa<sub>3</sub>N<sub>5</sub>.

**UV-vis Spectroscopy:** The solid-state UV-vis spectra of the powder CuTa<sub>3</sub>N<sub>5</sub> were measured on a Shimadzu UV-3600 Plus equipped with an integrating sphere. The diffuse reflection of the sample was measured in the range 200–1100 nm with barium sulphate as a reference. It was then transformed to absorption via the Kubelka-Munk function.<sup>[65]</sup> To record the UV-Vis spectra, the samples were placed between two microscope slides. The direct and indirect bandgaps were approximated by Tauc analysis.<sup>[66]</sup>

**X-Ray Diffraction (XRD):** PXRD measurements were performed in the Debye-Scherrer geometry with borosilicate glass capillaries (0.8 mm diameter) in a STOE Stadi P diffractometer equipped with a DECTRIS MYTHEN 1K detector and a curved Ge (111) monochromator using a Mo K<sub>α</sub> radiation source ( $\lambda \approx 0.70926$  Å). Variable temperature PXRD (VTPXRD) experiments were performed using an Oxford Habcryo-X Cryostream 700 Cobra for temperature regulation. The measurement range was from 2° to 64° (2 $\theta$ ) and the data were collected in the temperature range between 100 and 400 K. Pawley profile fit analysis<sup>[67]</sup> was carried out for all patterns at each temperature point by using TOPAS v6<sup>[68]</sup> to extract the lattice parameters (*a*, *b*, and *c*) and the volume (*V*), which are given in Table S1 (Supporting Information).

**High-Resolution Transmission Electron Microscopy (HR-TEM) with Energy Dispersive X-Ray Scattering (EDX):** High-resolution TEM images and analytical data were recorded in a double aberration-corrected Themis Z microscope (Thermo Fisher Scientific Electron Microscopy Solutions, Hillsboro, USA) equipped with a high-brightness FEG. An accelerating voltage of 200 kV was used. Aberration-corrected TEM images were recorded on a Gatan OneView CMOS camera (Gatan Inc., Pleasanton, USA). High-angle-annular dark-field (HAADF) scanning transmission electron microscopy (STEM) images were recorded with a Fischione Model 3000 detector with a semi-convergence angle of 21 mrad, a probe current of typically 50 pA, and an inner collection angle of 60.0 mrad. EDX hyperspectral data were obtained with a Super-X G2 four-segment SDD detector with a probe semi-convergence angle of 21 mrad and a beam current of approximately 200 pA. The EDX hyperspectral data were quantified with the Velox software (Thermo Fisher Scientific Electron Microscopy Solutions, Hillsboro, USA), through background subtraction and spectrum deconvolution.

**Raman Scattering:** Raman scattering measurements were performed using a home-built back-scattering system with a 785 nm CW diode laser (Toptica Inc., USA). The beam was focused on the sample with a 50X Zeiss objective. Elastic Rayleigh scattering was filtered by SureBlock Notch Filters (narrow band 785 nm) of Ondax Inc. and the scattered light was fo-

cused into a 1 m spectrometer (FHR 1000, Horiba) with a 600 grmm<sup>-1</sup> grating and detected by a CCD detector.

**Computational Methods:** All DFT calculations were performed with the periodic plane-wave code VASP (version 5.4.4).<sup>[69]</sup> Projector augmented wave (PAW)<sup>[70]</sup> potentials and Monkhorst-Pack *k*-point sampling were used.<sup>[71]</sup>

#### a) Geometry Optimizations

The structures were optimized with the Perdew–Burke–Ernzerhof (PBE)<sup>[72]</sup> functional including Tkatchenko–Scheffler (TS) dispersion corrections.<sup>[73]</sup> A 12 × 12 × 2 *k*-point grid and a cut-off energy of 750 eV was used for the geometry optimization of the conventional cell. Strict convergence criteria of 10<sup>-8</sup> eV and 10<sup>-3</sup> eVÅ<sup>-1</sup> were chosen for electronic and ionic optimizations, respectively. Structures were visualized with VESTA.<sup>[74]</sup>

#### b) Electronic-Structure Calculations

Electronic-structure calculations of the optimized structure were carried out with the hybrid functional HSE<sup>[59,60,75]</sup> with a cut-off of 750 eV and a 10 × 10 × 2 *k*-point grid, which was found to be sufficiently dense to numerically converge the electronic-structure data. The effect of spin-orbit coupling (SOC) was taken into account in non-collinear calculations on a reduced 7 × 7 × 2 *k*-point grid.

#### c) Harmonic-Phonon Calculations

Phonon densities of states (DOS) and dispersion relations were calculated with the phonoPy package<sup>[76]</sup> employing the finite-difference method. Displacements were created from a 4 × 4 × 2 supercell of the conventional cell, as well as from a 4 × 4 × 4 supercell of the primitive one. The supercell of the primitive cell was used in the case of computing the dielectric tensors and polarizabilities needed for Raman and IR spectra. *k*-point grids of 5 × 5 × 2 and 2 × 2 × 2 were used for supercell calculations of the conventional and primitive cells, respectively. Possible LO/TO splitting was accounted for by including non-analytic corrections in phonoPy and calculating the Born-effective charges in density functional perturbation theory.<sup>[77]</sup> The atomic motions corresponding to the phonon eigenvectors at different points in the Brillouin zone were visualized using ref. [78]. Harmonic-phonon Raman spectra were obtained by first selecting the active vibrational modes following symmetry selection rules, then computing the dielectric tensors and polarizabilities of the corresponding modes and plotting the spectra with the phonoPy-spectroscopy package.<sup>[79]</sup>

#### d) Potential Energy Surfaces

A mode mapping was done following the approach of Skelton et al.<sup>[49]</sup> The modemap tool was used,<sup>[80]</sup> which created a series of structures with displacements along the selected imaginary mode vectors in one or two dimensions. From single-point calculations of these structures, their energies were obtained to compute their corresponding potential energy surfaces. A 2 × 2 × 2 supercell of the primitive cell was used for computing the energies of the displacements, which was sufficient as it was commensurate with the *L*-point.

#### e) DFT-Based Molecular Dynamics

DFT-MD calculations of the NVT ensemble were carried out with a Nosé-Hoover thermostat. These calculations intrinsically account for anharmonic effects but neglect thermal variations of the lattice parameters. A 4 × 4 × 1 supercell of the conventional cell was used with 3 × 3 × 2 *k*-points, a 2 fs timestep and a trajectory of 32 ps after equilibration, which was  $\approx 3$ ps.

#### f) Vibrational Properties and Raman Spectra from MD

VDOS and Raman spectra were obtained from the velocity autocorrelation functions of the atomic positions and polarizabilities, which corresponds to an anharmonic treatment that was described in more detail in ref. [53]. For the Raman spectra, the polarizability of CuTa<sub>3</sub>N<sub>5</sub> was computed at every 10<sup>th</sup> MD step (time interval: 20 fs) and found a trajectory of 13 ps to be sufficiently long. According to the Nyquist–Shannon sampling theorem, the interval was sufficient to capture all frequency information up to 834 cm<sup>-1</sup>.<sup>[81]</sup> Intensities were spherically averaged over all orientations and summed over all polarization directions to allow for comparison with experiment. For plotting smoother spectra, Lorentzian broadening with  $\gamma = 2.6$  cm<sup>-1</sup> was used.

The atomic displacements according to a given frequency range were obtained using a frequency filter. In brief, the time-dependent atomic positions were Fourier-transformed to obtain the velocity autocorrelation function, a band-pass filter was applied, and then Fourier-transformed back to obtain the time-dependent atomic coordinates along the trajectory according to the frequency window.

#### i) Effective Dynamic Potential Wells

To calculate the effective potential,  $U_{\text{dyn}}$ , in which a given atom moves along the MD, a Boltzmann-inversion technique was used. The effective dynamic potential of a given atom,  $U_{\text{dyn}}$  is calculated by:

$$U_{\text{dyn}}(u) = k_B T \ln P(u) \quad (2)$$

where  $u$  is a displacement of a given atom,  $T$  is temperature,  $k_B$  the Boltzmann constant, and  $P(u)$  a histogram of atomic displacements. In this way, one obtains an effective dynamic potential well that includes the effects of populated vibrational modes and their anharmonicity according to the MD run.

## Supporting Information

Supporting Information is available from the Wiley Online Library or from the author.

## Acknowledgements

This work received support from the Alexander von Humboldt-Foundation in the framework of the Sofja Kovalevskaja Award, endowed by the German Federal Ministry of Education and Research, by the Deutsche Forschungsgemeinschaft via the Walter-Benjamin Programme (HE 8878/1-1) and via Germany's Excellence Strategy - EXC 2089/1-390776260, by TUM.solar in the context of the Bavarian Collaborative Research Project Solar Technologies Go Hybrid (SolTech), and by the European Research Council (ERC) under the European Union's Horizon 2020 research and innovation programme (grant agreement No. 864234 and No. 850041). Furthermore, the authors acknowledge support by the Technical University of Munich - Institute for Advanced Study, funded by the German Excellence Initiative and the European Union Seventh Framework Programme under Grant Agreement No. 291763. The authors further acknowledge the Gauss Centre for Supercomputing e.V. for funding this project by providing computing time through the John von Neumann Institute for Computing on the GCS Supercomputer JUWELS at Jülich Supercomputing Centre.

Open access funding enabled and organized by Projekt DEAL.

## Conflict of Interest

The authors declare no conflict of interest.

## Data Availability Statement

The data that support the findings of this study are available from the corresponding author upon reasonable request.

## Keywords

anharmonic lattice dynamics, molecular dynamics, nitrides, optoelectronic properties, raman spectroscopy

Received: September 12, 2023

Revised: January 22, 2024

Published online: March 30, 2024

- [1] P. Yu, M. Cardona, *Fundamentals of Semiconductors: Physics and Materials Properties*, Graduate Texts in Physics, Springer, Berlin Heidelberg, 2010.
- [2] M. T. Dove, *Introduction to Lattice Dynamics*, vol. 4, Cambridge University Press, Cambridge 1993.
- [3] F. Giustino, *Rev. Mod. Phys.* **2017**, *89*, 015003.
- [4] M. Asher, D. Angerer, R. Korobko, Y. Diskin-Posner, D. A. Egger, O. Yaffe, *Adv. Mater.* **2020**, *32*, 1908028.
- [5] C. E. Patrick, K. W. Jacobsen, K. S. Thygesen, *Phys. Rev. B* **2015**, *92*, 201205.
- [6] J. Wiktorski, U. Rothlisberger, A. Pasquarello, *J. Phys. Chem. Lett.* **2017**, *8*, 5507.
- [7] C. Katan, A. D. Mohite, J. Even, *Nat. Mater.* **2018**, *17*, 377.
- [8] D. A. Egger, A. Bera, D. Cahen, G. Hodes, T. Kirchartz, L. Kronik, R. Lovrincic, A. M. Rappe, D. R. Reichman, O. Yaffe, *Adv. Mater.* **2018**, *30*, 1800691.
- [9] M. Z. Mayers, L. Z. Tan, D. A. Egger, A. M. Rappe, D. R. Reichman, *Nano Lett.* **2018**, *18*, 8041.
- [10] C. Gehrman, D. A. Egger, *Nat. Commun.* **2019**, *10*, 1.
- [11] X.-G. Zhao, G. M. Dalpian, Z. Wang, A. Zunger, *Phys. Rev. B* **2020**, *101*, 155137.
- [12] T. Lanigan-Atkins, X. He, M. J. Krogstad, D. M. Pajeroski, D. L. Abernathy, G. N. M. N. Xu, Z. Xu, D.-Y. Chung, M. G. Kanatzidis, S. Rosenkranz, R. Osborn, O. Delaire, *Nat. Mater.* **2021**, *20*, 977.
- [13] M. J. Schilcher, P. J. Robinson, D. J. Abramovitch, L. Z. Tan, A. M. Rappe, D. R. Reichman, D. A. Egger, *ACS Energy Lett.* **2021**, *6*, 2162.
- [14] M. Zacharias, G. Volonakis, F. Giustino, J. Even, *npj Comput. Mater.* **2023**, *9*, 153.
- [15] S. A. Seidl, X. Zhu, G. Reuveni, S. Aharon, C. Gehrman, S. Caicedo-Dávila, O. Yaffe, D. A. Egger, *Phys. Rev. Mater.* **2023**, *7*, L09240.
- [16] M. J. Schilcher, D. J. Abramovitch, M. Z. Mayers, L. Z. Tan, D. R. Reichman, D. A. Egger, *Phys. Rev. Mater.* **2023**, *7*, L081601.
- [17] J.-J. Zhou, O. Hellman, M. Bernardi, *Phys. Rev. Lett.* **2018**, *121*, 226603.
- [18] M. Zacharias, M. Scheffler, C. Carbogno, *Phys. Rev. B* **2020**, *102*, 045126.
- [19] Y.-N. Wu, W. A. Saidi, J. K. Wuenschell, T. Tadano, P. Ohodnicki, B. Chorpene, Y. Duan, *J. Phys. Chem. Lett.* **2020**, *11*, 2518.
- [20] E. S. Božin, C. D. Malliakas, P. Souvatzis, T. Proffen, N. A. Spaldin, M. G. Kanatzidis, S. J. Billinge, *Science* **2010**, *330*, 1660.
- [21] C. Kastl, P. Bonfà, L. Maserati, *Adv. Opt. Mater.* **2023**, *11*, 2202213.
- [22] R. A. Cowley, *Rep. Prog. Phys.* **1968**, *31*, 123.
- [23] C. C. Stoumpos, C. D. Malliakas, M. G. Kanatzidis, *Inorg. Chem.* **2013**, *52*, 9019.
- [24] A. N. Beecher, O. E. Semonin, J. M. Skelton, J. M. Frost, M. W. Terban, H. Zhai, A. Alatas, J. S. Owen, A. Walsh, S. J. L. Billinge, *ACS Energy Lett.* **2016**, *1*, 880.
- [25] F. Wang, W. Chu, L. Huber, T. Tu, Y. Dai, J. Wang, H. Peng, J. Zhao, X.-Y. Zhu, *Proc. Natl. Acad. Sci. U.S.A.* **2022**, *119*, 2122436119.
- [26] F. J. DiSalvo, S. J. Clarke, *Curr. Opin. Solid State Mater. Sci.* **1996**, *1*, 241.
- [27] W. Sun, C. J. Bartel, E. Arca, S. R. Bauers, B. Matthews, B. Orvañanos, B.-R. Chen, M. F. Toney, L. T. Schelhas, W. Tumas, J. Tate, A. Zakutayev, S. Lany, A. M. Holder, G. Ceder, *Nat. Mater.* **2019**, *18*, 732.
- [28] A. Ścigała, E. Szyk, L. Dobrzańska, D. H. Gregory, R. Szczepny, *Coord. Chem. Rev.* **2021**, *436*, 213791.
- [29] A. L. Greenaway, C. L. Melamed, M. B. Tellekamp, R. Woods-Robinson, E. S. Toberer, J. R. Neilson, A. C. Tamboli, *Annu. Rev. Mater. Res.* **2021**, *51*, 591.
- [30] O. C. Gagné, *Chem. Sci.* **2021**, *12*, 4599.
- [31] C. M. Caskey, R. M. Richards, D. S. Ginley, A. Zakutayev, *Mater. Horiz.* **2014**, *1*, 424.
- [32] Y. Inoue, M. Nomiya, O. Takai, *Vacuum* **1998**, *51*, 673.

- [33] C. M. Caskey, A. Holder, S. Shulda, S. T. Christensen, D. Diercks, C. P. Schwartz, D. Biagioni, D. Nordlund, A. Kukliansky, A. Natan, D. Prendergast, B. Orvananos, W. Sun, X. Zhang, G. Ceder, D. S. Ginley, W. Tumas, J. D. Perkins, V. Stevanovic, S. Pylypenko, S. Lany, R. M. Richards, A. Zakutayev, *J. Chem. Phys.* **2016**, *144*, 14.
- [34] A. Bikowski, S. Siol, J. Gu, A. Holder, J. S. Mangum, B. Gorman, W. Tumas, S. Lany, A. Zakutayev, *Chem. Mater.* **2017**, *29*, 6511.
- [35] M. Yang, A. Zakutayev, J. Vidal, X. Zhang, D. S. Ginley, F. J. DiSalvo, *Energy Environ. Sci.* **2013**, *6*, 2994.
- [36] A. Zakutayev, A. J. Allen, X. Zhang, J. Vidal, Z. Cui, S. Lany, M. Yang, F. J. DiSalvo, D. S. Ginley, *Chem. Mater.* **2014**, *26*, 4970.
- [37] A. Zakutayev, *J. Mater. Chem. A* **2016**, *4*, 6742.
- [38] I. Ohkubo, T. Mori, *Chem. Mater.* **2015**, *27*, 7265.
- [39] W. Shockley, H. J. Queisser, *J. Appl. Phys.* **1961**, *32*, 510.
- [40] C.-M. Jiang, S. E. Reyes-Lillo, Y. Liang, Y.-S. Liu, G. Liu, F. M. Toma, D. Prendergast, I. D. Sharp, J. K. Cooper, *Chem. Mater.* **2019**, *31*, 2524.
- [41] N. J. Szymanski, L. Walters, O. Hellman, D. Gall, S. V. Khare, *J. Mater. Chem. A* **2018**, *6*, 20852.
- [42] U. Zachwieja, H. Jacobs, *Eur. J. Inorg. Chem.* **1991**, *28*, 1055.
- [43] *International Tables for Crystallography. Volume A: Space-Group Symmetry*, International Union of Crystallography, Chester **2002**, <https://doi.org/10.1107/97809553602060000100>.
- [44] I. Pallikara, P. Kayastha, J. M. Skelton, L. D. Whalley, *Electron. Struct.* **2022**, *4*, 033002.
- [45] R. X. Yang, J. M. Skelton, E. L. Da Silva, J. M. Frost, A. Walsh, *J. Phys. Chem. Lett.* **2017**, *8*, 4720.
- [46] A. Marronnier, H. Lee, B. Geffroy, J. Even, Y. Bonnassieux, G. Roma, *J. Phys. Chem. Lett.* **2017**, *8*, 2659.
- [47] J. Klarbring, *Phys. Rev. B* **2019**, *99*, 104105.
- [48] J. M. Skelton, D. Tiana, S. C. Parker, A. Togo, I. Tanaka, A. Walsh, *J. Chem. Phys.* **2015**, *143*, 064710.
- [49] J. M. Skelton, L. A. Burton, S. C. Parker, A. Walsh, C.-E. Kim, A. Soon, J. Buckeridge, A. A. Sokol, C. R. A. Catlow, A. Togo, I. Tanaka, *Phys. Rev. Lett.* **2016**, *117*, 075502.
- [50] L. D. Whalley, J. M. Skelton, J. M. Frost, A. Walsh, *Phys. Rev. B* **2016**, *94*, 220301.
- [51] J. Klarbring, O. Hellman, I. A. Abrikosov, S. I. Simak, *Phys. Rev. Lett.* **2020**, *125*, 045701.
- [52] M. T. Dove, *Am. Min.* **1997**, *82*, 213.
- [53] M. Thomas, M. Brehm, R. Fligg, P. Vöhringer, B. Kirchner, *Phys. Chem. Chem. Phys.* **2013**, *15*, 6608.
- [54] X. Zhu, S. Caicedo-Dávila, C. Gehrman, D. A. Egger, *ACS Appl. Mater. Interf.* **2022**, *14*, 22973.
- [55] M. Menahem, N. Benshalom, M. Asher, S. Aharon, R. Korobko, O. Hellman, O. Yaffe, *Phys. Rev. Mater.* **2023**, *7*, 044602.
- [56] J. Li, A. Sleight, C. Jones, B. Toby, *J. Solid State Chem.* **2005**, *178*, 285.
- [57] M. T. Dove, H. Fang, *Rep. Prog. Phys.* **2016**, *79*, 066503.
- [58] T. A. Bird, M. G. Wilkinson, D. A. Keen, R. I. Smith, N. C. Bristowe, M. T. Dove, A. E. Phillips, M. S. Senn, *Phys. Rev. B* **2021**, *104*, 214102.
- [59] J. Heyd, G. E. Scuseria, M. Ernzerhof, *J. Chem. Phys.* **2003**, *118*, 8207.
- [60] A. V. Krukau, O. A. Vydrov, A. F. Izmaylov, G. E. Scuseria, *J. Chem. Phys.* **2006**, *125*, 22.
- [61] B. Monserrat, *Phys. Rev. B* **2016**, *93*, 100301.
- [62] A. Zakutayev, C. M. Caskey, A. N. Fioretti, D. S. Ginley, J. Vidal, V. Stevanovic, E. Tea, S. Lany, *J. Phys. Chem. Lett.* **2014**, *5*, 1117.
- [63] C.-M. Jiang, L. I. Wagner, M. K. Horton, J. Eichhorn, T. Rieth, V. F. Kunzelmann, M. Kraut, Y. Li, K. A. Persson, I. D. Sharp, *Mater. Horiz.* **2021**, *8*, 1744.
- [64] J. Eichhorn, S. P. Lechner, C.-M. Jiang, G. F. Heunecke, F. Munnik, I. D. Sharp, *J. Mater. Chem. A* **2021**, *9*, 20653.
- [65] P. Kubelka, F. Munk, *Z. Tech. Phys.* **1931**, *12*, 259.
- [66] J. Tauc, *Mater. Res. Bull.* **1968**, *3*, 37.
- [67] G. Pawley, *J. Appl. Crystallogr.* **1981**, *14*, 357.
- [68] A. A. Coelho, *J. Appl. Crystallogr.* **2018**, *51*, 210.
- [69] G. Kresse, J. Furthmüller, *Phys. Rev. B* **1996**, *54*, 11169.
- [70] G. Kresse, D. Joubert, *Phys. Rev. B* **1999**, *59*, 1758.
- [71] H. J. Monkhorst, J. D. Pack, *Phys. Rev. B* **1976**, *13*, 5188.
- [72] J. P. Perdew, K. Burke, M. Ernzerhof, *Phys. Rev. Lett.* **1996**, *77*, 3865.
- [73] A. Tkatchenko, M. Scheffler, *Phys. Rev. Lett.* **2009**, *102*, 073005.
- [74] K. Momma, F. Izumi, *J. Appl. Crystallogr.* **2011**, *44*, 1272.
- [75] J. Heyd, G. E. Scuseria, *J. Chem. Phys.* **2004**, *120*, 7274.
- [76] A. Togo, I. Tanaka, *Scr. Mater.* **2015**, *108*, 1.
- [77] M. Gajdoš, K. Hummer, G. Kresse, J. Furthmüller, F. Bechstedt, *Phys. Rev. B* **2006**, *73*, 045112.
- [78] H. Miranda, Phonon website, <http://henriquemiranda.github.io/phononwebsite/phonon.html> (accessed: September 2023).
- [79] J. M. Skelton, L. A. Burton, A. J. Jackson, F. Oba, S. C. Parker, A. Walsh, *Phys. Chem. Chem. Phys.* **2017**, *19*, 12452.
- [80] J. M. Skelton, Modemap, <https://github.com/JMSkelton/ModeMap>, **2022** (accessed: September 2023).
- [81] C. E. Shannon, *Proc. IRE* **1949**, *37*, 10.